The International Journal of Advanced Manufacturing Technology
https://doi.org/10.1007/s00170-024-14457-z

ORIGINAL ARTICLE

Material removal characterization during axial ultrasonic vibration grinding SiC_p/Al composites with a single diamond grain

Jianhao Peng[1] · Yu Yao[1] · Zhipeng Xu[2] · Xuebin Yao[1] · Biao Zhao[1] · Wenfeng Ding[1]

Received: 7 May 2024 / Accepted: 6 September 2024
© The Author(s), under exclusive licence to Springer-Verlag London Ltd., part of Springer Nature 2024

Abstract
Silicon carbide particle-reinforced aluminum matrix composites (SiC_p/Al) have found extensive use in electronic packaging, aircraft manufacturing, and various other industries due to their exceptional strength, low density, and high wear resistance. Nevertheless, owing to the multiphase microstructure resulting from SiC particles embedded in an Al matrix, the presence of non-ideal regions within the material poses a significant challenge in achieving high surface integrity. Ultrasonic vibration-assisted grinding (UVAG) has been proven to be an effective machining technique for improving the machinability of reinforced particles. The axial ultrasonic vibration grinding with a single diamond grain was conducted to realize the material removal mechanism of SiC_p/Al composites. Furthermore, a 3D model of diamond grains with a cohesive force unit was constructed to simulate the material removal evolution of SiC particles under UVAG. Results demonstrate that the utilization of ultrasonic vibration-assisted grinding facilitates the plastic-like removal of hard particles and promotes the transformation of brittle SiC material removal into a plasticized form. UVAG could effectively mitigate the occurrence of pit formation caused by SiC particles, which would otherwise result from extensive crushing and detachment during the conventional grinding process, thus, enhancing the integrity of the machined surface.

Keywords Ultrasonic vibration-assisted grinding · Grinding force · Material removal mechanism · SiC_p/Al composites · Machined surface damage

1 Introduction

Silicon carbide particle-reinforced aluminum matrix composites (SiC_p/Al) consist of ductile Al metals and brittle SiC ceramics, which exhibit intricate spatial structure and reinforced matrix interfaces. Their superior mechanical qualities, including high specific strength and specific modulus, low coefficient of expansion, fatigue resistance, wear resistance, and good reliability, among other excellent qualities [1], indicate good application prospects in electronic packaging, precision optical instruments, aerospace, and other fields [2, 3]. The grinding process is usually the final and key step to achieve precision machining of difficult-to-machine materials and key components. However, the high hardness and brittleness of SiC particles and the high adhesion of the Al substrate bring great difficulties to mechanical processing [4]. During grinding, the grinding wheel and abrasive particles are subjected to alternating impact loads from reinforced particles and adhesion from viscous metals, resulting in rapid wear and blockage of the grinding wheel and complex processing damage [5], which seriously affects the processing quality and efficiency and is one of the challenges limiting the application of SiC_p/Al composites in high-end equipment. In conventional processing, composite materials undergo a complex removal process due to the extrusion and shearing effects of abrasive particles. Common forms of processing damage include the extraction of SiC particles, resulting in the formation of holes, the fragmentation and formation of cracks in SiC particles, as well as tearing and coating of the Al alloy substrate [6–10].

Ultrasonic vibration-assisted machining (UVAM) [11, 12] is a process that utilizes piezoelectric effects to impart high-frequency, regular vibrations to tools during ordinary machining operations. For grinding, it can be categorized

✉ Biao Zhao
zhaobiao@nuaa.edu.cn

1 National Key Laboratory of Science and Technology On Helicopter Transmission, Nanjing University of Aeronautics and Astronautics, Nanjing 210016, China

2 AVIC Changhe Aircraft Industry (Group) Co., Ltd, AVIC China, Jingdezhen 333002, China

Published online: 19 September 2024

into UVAG on the end face and lateral surface, depending on the motion of the grinding wheel. Most previous studies have concentrated on UVAG on the end face, whereas this study primarily focuses on the latter. UVAM has a significant impact on the formation of machining damage and the quality of the machined surface. Zhou et al. [5] employed a rotary ultrasonic surface grinding process to treat SiC_p/Al composites with a medium particle size ratio. With the novel method, wheel obstruction and grinding surface burns were less frequent than with traditional grinding, and there was a reduction of over 10% in both the average grinding force and the surface roughness value. Ying et al. [13] investigated the influence of grinding parameters on UVAG of SiC_p/Al. Researchers hypothesized that different vibration characteristics would produce varying surface textures on the machined surface, significantly affecting its surface roughness. Ultrasonic amplitude was the most crucial factor influencing the surface roughness of the machined surface. Under an appropriate ultrasonic amplitude (2 μm), the surface roughness achieved a minimum value of 0.151 μm.

The abrasive grain grinding test [14] is an important means to study the material removal mechanism in the grinding process of SiC_p/Al composites. Du et al. [15] conducted a single abrasive grain grinding test on SiC_p/Al composites and found that during the material removal process, SiC particles exhibited removal methods such as crushing, fracture, microcracking, shearing, and pull-out, while the Al matrix underwent significant plastic deformation. Additionally, the removal of SiC particles by shearing can reduce particle crushing and internal cracks. Feng et al. [16] discovered that SiC underwent partial plastic removal during the UVAG process of a 62% SiC_p/Al composite. However, there remains some controversy regarding whether ultrasonic vibration can induce brittle-plastic transition in brittle materials during the mechanical removal process of particle-reinforced Al matrix composites. Zhang et al. [17] established a critical cutting thickness model for the brittle–ductile transition of hard brittle materials under UVAG and studied the effect of the cutting thickness of a single abrasive grain on grinding specific energy. Lu et al. [18] constructed a mathematical model based on cutting energy and believed that there was a brittle-plastic transition in the cutting mode during the cutting process of SiC_p/Al material. Zheng et al. [19] performed scratch tests on a 45% SiC_p/Al composite using both traditional cutting methods and UVAM methods and found no obvious brittle-plastic transition. Nevertheless, the beneficial effects of ultrasonic-assisted machining have been confirmed by numerous studies [20–22]. Zha et al. [23] compared the cutting force, friction coefficient, and scratch morphology of SiC_p/Al composites under ultrasonic vibration-assisted cutting and conventional cutting conditions. The results indicated that the cutting force and friction coefficient under UVAM were lower, thereby reducing the adhesion of Al alloys.

Most of the above research focused on machining, and the causes of machining damage in SiC_p/Al composites were analyzed through planar simulations. However, research on the material removal mechanism of 3D axial UVAG is still relatively scarce. The material removal mechanism under ultrasonic conditions and the interaction process between different phases require further investigation and elucidation. Section 2 presents the UVAG system, its simulation model, and experimental preparations in detail. Subsequently, Section 3 delves into the removal processes of SiC_p/Al composites under varying grinding speeds, with particular emphasis on changes in grinding force and scratch morphology. The evolution of material removal processes of SiC particles under UVAG was simulated using the simulation model, and the resulting changes in grinding force and scratch morphology were analyzed and discussed. Finally, the conclusions were synthesized based on the aforementioned findings. This study provides a theoretical foundation for the effective removal and high surface integrity control of SiC_p/Al composites, thereby supporting the engineering application of UVAG.

2 Experiment setup

2.1 Workpiece material

The particle-reinforced metal matrix composite used in this paper was based on Al alloy, and SiC particles were added into it by stirring casting. The SiC_p/Al interface produced by this preparation method had good bonding properties. The statistical results of microstructure and particle size under scanning electron microscope (SEM) are shown in Fig. 1. The volume fraction of the SiC phase was 60 vol.%. The particle sizes were calculated by ImageJ software, and the main SiC particle size was 21–29 μm (proportion of particle area).

2.2 Experimental setup and setup

Figure 2 shows a grinding test using diamond abrasive grains on the five-axis ultrasonic machining center DMG Ultrasonic 20 linear. The acoustic emission test device (Diesel AE6000) was used to accurately monitor the tool setting process; two diamond abrasive grains with a size of 40/50# and Cu-Sn-Ti alloy were fixed on the cylindrical surface of the stepped shaft (symmetrically distributed) by high-temperature brazing, ensuring that the entire process was carried out in a high-temperature vacuum furnace. The workpiece, measuring 24 mm × 12 mm × 10 mm, was carefully ground and polished prior to the experiment to reduce the influence of the initial workpiece surface morphology

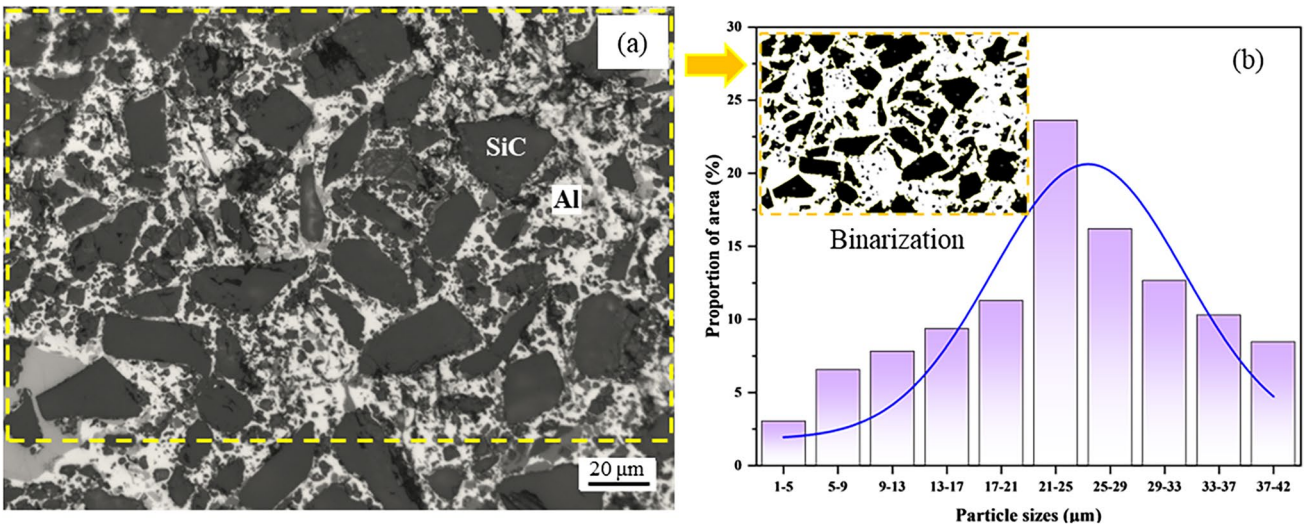

Fig. 1 Microstructure morphology of SiC_p/Al and statistical diagram of SiC particles: **a** SEM images of SiC_p/Al and **b** SiC particle size distribution counted by proportion of the particle area

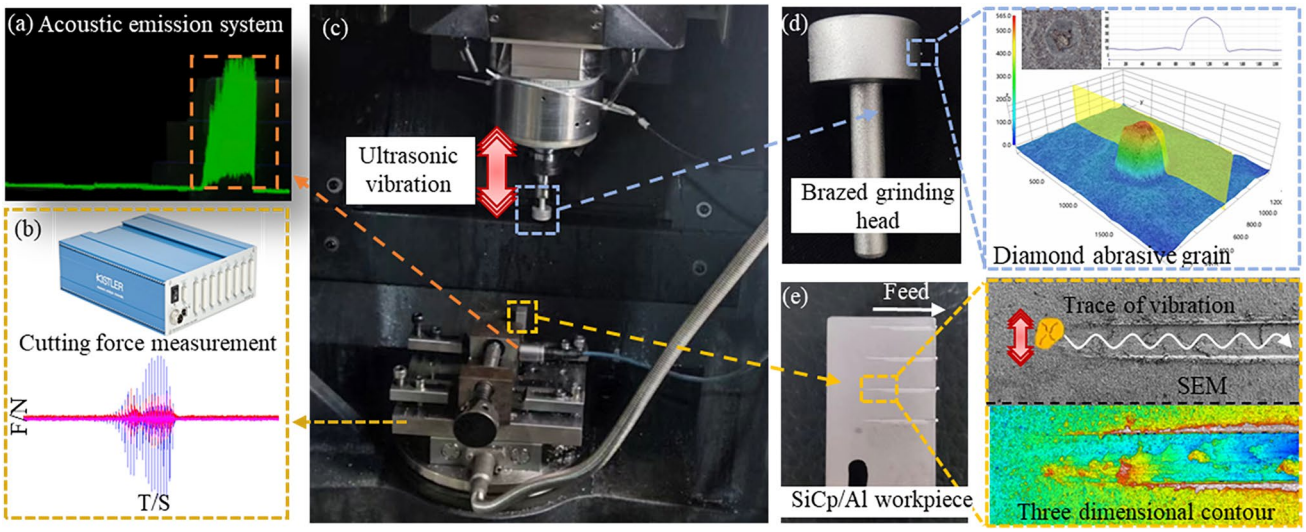

Fig. 2 UVAG and CG test platform: **a** acoustic emission test device, **b** cutting force test device, **c** DMG Ultrasonic 20 linear, **d** brazed grinding head, and **e** scratch morphology of sample after grinding

on subsequent scratch examination. The grinding force in the UVAG process was obtained using the Kistler 9129AA three-component dynamometer, which transmitted the data to a PC through a 5070A charge amplifier and 5167A data acquisition card, where it was analyzed by DynoWare. The COXEM EM-30 PLUS scanning electron microscope (SEM) and 3D video microscope were used to observe the surface morphology of the workpiece after grinding. Figure 3 is the schematic diagram of UVAG and CG processes, showing the micromachining tracks produced by these processes. The UVAG test was conducted without coolant, and the specific parameters are shown in Table 1.

2.3 Simulation settings

2.3.1 Simulation model

To further reveal the formation and evolution process of material removal and machined surface damage, the contact state with Al- and SiC-reinforced particles during diamond abrasive grain grinding was analyzed, and a 3D model of SiC_p/Al grinding by a single diamond with cohesive force unit was established. ABAQUS software was used to simulate the grinding process, in which the cutting workpiece material was SiC_p/Al composite (the size was 200 × 50 × 50

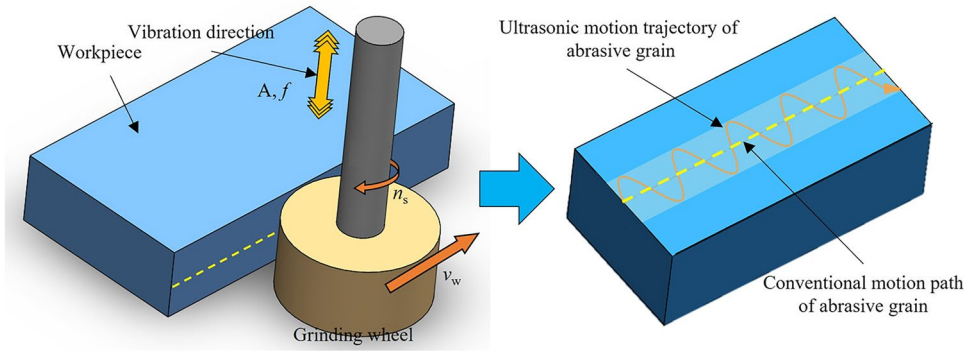

Fig. 3 Schematic and micromachining trajectory under both UVAG and CG

Table 1 Test parameters of UVAG (ultrasonic power 30%) and CG (ultrasonic power 0%)

Parameter	Value
Spindle speed n_s (r/min)	5000, 7500, 10,000, 12,500
Grinding speed v_s (m/s)	5.23, 7.85, 10.47, 13.08
Workpiece speed v_w (mm/min)	40
Depth of cut a_p (mm)	0.02
Frequency f (kHz)	28.3
Ultrasonic power	0, 30%

μm). To further analyze the influence of abrasive particles on SiC particle distribution at different relative positions, the SiC distribution was set to have a linear law (Fig. 4). The matrix and particle were defined, respectively, and the cohesive element between the two phases was set as the contact interface.

In order to simulate the engraving process more concisely, the diamond abrasive particles were simplified into a cone structure with a particle size of 56 μm and a cone angle of 60° and set as a rigid body. In the simulation analysis, the tip part can fully simulate the machining state of the abrasive micro-cutting edge in grinding. The SiC particles were simplified as spheres (26 μm). According to the different positions of abrasive particles acting on SiC particles, the scratch removal processes of SiC_p/Al composites were analyzed, as shown in Fig. 4.

2.3.2 Material constitutive and damage model

In the finite element method (FEM) analysis, the correctness of the material constitutive model has an important impact on the accuracy of the simulation results. Choosing the appropriate material constitutive model is the key to ensuring the success of FEM simulation. Therefore, it is necessary to assign different material properties to the Al alloy matrix, SiC particles, and cohesive unit interface layer.

(1) Al alloy matrix. Al alloy is a metal with good ductility, which is prone to thermal deformation in the process of high strain and high strain rate cutting, so it is regarded as a thermoplastic material [24], and its basic physical parameters are shown in Table 2.

In this study, the Johnson–Cook constitutive model is used to conduct the characterization simulation research. The flow stress in the Johnson–Cook (J–C) model of Al alloy can be expressed by Eq. (1), and the parameters of the J–C constitutive model are shown in Table 3.

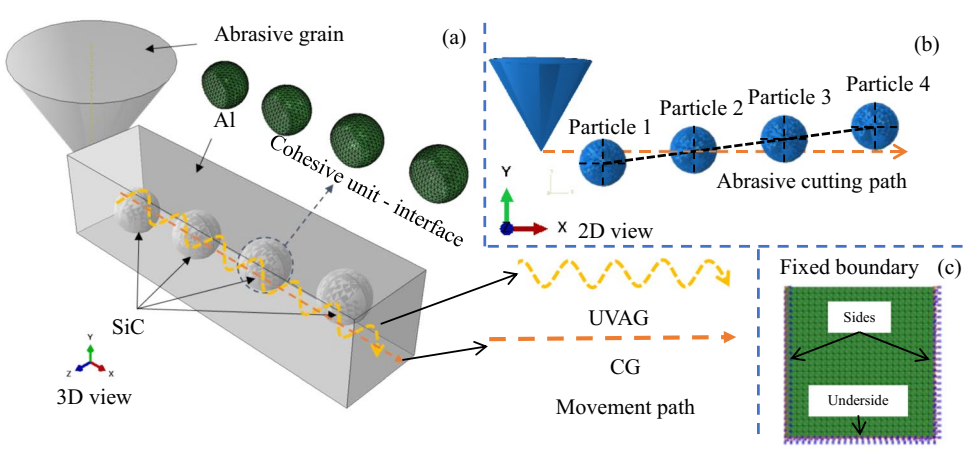

Fig. 4 3D model of single-diamond grinding SiC_p/Al composite: **a** 3D view of the model assembly containing 0-thickness cohesive element (green mesh structure), **b** relative distribution of abrasive particles and SiC particles in 2D view, and **c** boundary fixation conditions of SiC_p/Al model

Table 2 Basic physical properties of SiC_p/Al composite and diamond abrasive [25–27]

Material type	Elasticity (MPa)	Poisson's ratio	Density (kg/m^3)	Conductivity (W/m·K)
Al	75,000	0.33	2850	175
SiC	420,000	0.17	3186	81
Diamond	1,220,000	0.07	3515	22

Table 3 J-C constitutive model parameters of Al [28]

A	B	C	n	m	T_{room}	T_{melt}
224	426	0.002	0.2	0.859	20	900

Table 4 JC damage model parameters of Al alloys [25]

D_1	D_2	D_3	D_4	D_5
0.13	0.13	−1.5	0.011	0

$$\sigma = [A + B\varepsilon^2][1 + C\ln\frac{\dot{\varepsilon}}{\dot{\varepsilon}_0}][1 - (\frac{T - T_{room}}{T_{melt} - T_{room}})] \quad (1)$$

where σ is the equivalent flow stress, A, B, C, n, and m are the yield strength, hardening modulus, strain rate sensitivity coefficient, work hardening index, and thermal softening coefficient, respectively. $\dot{\varepsilon}$ and $\dot{\varepsilon}_0$ represent the reference strain rate and the equivalent plastic strain. T, T_{room}, and T_{melt} are workpiece temperature, material melting point, and room temperature, respectively.

In this paper, the material failure mode of the Al matrix is defined by the Johnson–Cook failure criterion, and its equation is:

$$\omega = \sum \frac{\Delta\bar{\varepsilon}}{\bar{\varepsilon}_f} \quad (2)$$

$$\bar{\varepsilon}_f = [D_1 + D_2 exp(D_3\frac{P}{\sigma})](1 + D_4 ln\frac{\dot{\varepsilon}}{\dot{\varepsilon}_0})(1 + D_5\frac{T - T_{room}}{T_{melt} - T_{room}}) \quad (3)$$

where $\Delta\bar{\varepsilon}$ is the increment of equivalent plastic strain, $\bar{\varepsilon}_f$ is the failure equivalent strain of the material, and ω is the failure parameter, with an initial value of 0. When the failure parameter reaches 1, the workpiece material fails. D_1–D_5 represent the damaged parameter [25], as shown in Table 4.

(2) SiC particles. JH-2 material constitutive model has been widely used in the study of material failure of hard and brittle materials. It mainly consists of three parts: strength model equation, separation criterion equation, and state equation. SiC has the properties of hard and brittle materials, so the relevant property parameters of the material were determined by the JH-2 material model property parameters [29]. The specific parameter properties are shown in Table 5.

(3) Cohesive force unit. The transfer of force between the Al matrix and SiC particles in SiC_p/Al composites not only has a significant impact on material properties but also plays an important role in the cutting process. To better simulate the interaction between the Al matrix and SiC particles, a cohesive force model was established [30], and the constitutive relationship of the cohesive force model is shown in Fig. 5.

According to the law of traction separation, the stiffness of the cohesive force element decreases with increasing displacement until the stiffness reaches 0, and the cohesive force element completely fails. The first stage is the initial damage, and the second stage is the damage evolution process. The bonding element model can be represented as:

$$t_{ra} = \begin{Bmatrix} t_n \\ t_s \\ t_t \end{Bmatrix} = \begin{Bmatrix} K_{nn} & K_{ns} & K_{nt} \\ K_{ns} & K_{ss} & K_{st} \\ K_{nt} & K_{st} & K_{tt} \end{Bmatrix} \begin{Bmatrix} \delta_n \\ \delta_s \\ \delta t \end{Bmatrix} = K\delta \quad (4)$$

where t_{ra} represents the traction force, n, s, and t represent the normal direction and shear direction, respectively. K_{nn}, K_{ns}, and K_{nt} respectively represent normal stiffness and tangential stiffness. δ_n, δ_s, and δ_t represent the initial damage displacement.

The maximum stress damage criterion is used to describe the initiation of damage in cohesive elements, and its expression is:

Table 5 JH-2 material model parameters of SiC [29]

A	B	C	M	N	D_1	D_2	K_1	K_2	K_3
0.96	0.35	0.009	1.0	0.65	0.48	0.48	220	361	0

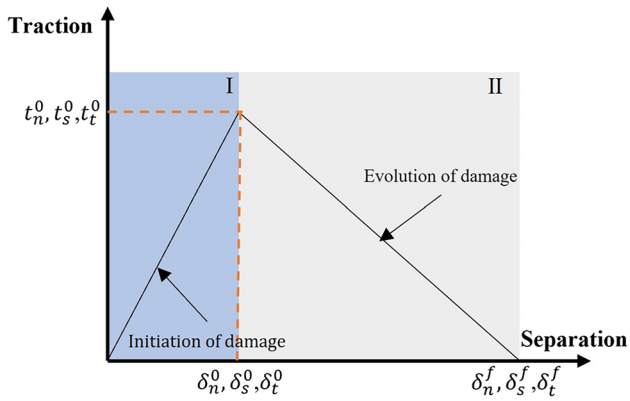

Fig. 5 Traction separation model of cohesive units

$$\max\left\{\frac{\langle\sigma_n\rangle}{N_{\max}}, \frac{\sigma_s}{S_{\max}}, \frac{\sigma_t}{T_{\max}}\right\} = 1 \tag{5}$$

where σ_n is the normal component of stress, σ_s and σ_t are the tangential component of stresses, $N_{\max}$ is the maximum nominal stress in the normal direction, and $S_{\max}$ and $T_{\max}$ are the maximum nominal stresses in the tangential direction.

Other conditions for simulation analysis: grinding speed $v_s = 5.23$ m/s; depth of cut $a_p = 30$ μm, the vibration amplitude $A = 2$ μm, and the vibration frequency $f = 28.3$ kHz. Due to the high hardness of the tool made of diamond material, it has been simplified as a rigid body to improve computational efficiency. In this study, the contact form between the tool and the workpiece in the simulation was face-to-face contact, and normal friction was defined as frictionless hard contact, while tangential friction was defined as penalty friction, with a friction coefficient set to 0.3.

3 Results and discussion

3.1 Influence of spindle speed on material removal mechanism

3.1.1 Grinding force

The comparison of grinding forces between UVAG and CG under different grinding speeds is shown in Fig. 6a–c, where the grinding forces were taken as the maximum values measured. Figure 6a shows the influence of spindle speed on radial grinding force F_x, which indicated that for CG, the grinding force exhibited a trend of first decreasing and then increasing, with the minimum radial force occurring at a grinding speed of 7.85 m/s, at which point F_x was 23.51 N. For UVAG, the grinding force exhibited a gradual decrease trend, but the overall change was not significant, with the minimum radial force occurring at a grinding speed of 13.08 m/s, at which point F_x was 3.04 N. Figure 6b shows the influence of grinding speed on tangential grinding force F_y, which indicated that for CG, the grinding force exhibited a trend of first decreasing and then increasing, with the minimum radial force occurring at a grinding speed of 7.85 m/s, at which point F_y was 13.62 N. For UVAG, the grinding force exhibited a gradual decrease trend, with the minimum radial force occurring at a grinding speed of 13.08 m/s, at which point F_y was 2.18 N. Figure 6c shows the influence of grinding speed on axial grinding force F_z, which indicated that for CG, the grinding force also exhibited a trend of first decreasing and then increasing, with the minimum radial force occurring at a grinding speed of 7.85 m/s, at which point F_y was 10.22 N. For UVAG, the grinding force exhibited a trend of first decreasing and then slowly increasing, with the minimum radial force occurring at a grinding speed of 7.85 m/s, at which point F_z was 2.82 N. It can be seen that the grinding speed had a significant impact on CG grinding forces, with a grinding speed of 7.85 m/s being the optimal speed. The influence of grinding speed on UVAG grinding forces was relatively small. In comparison, ultrasonic vibration greatly reduced the grinding force in all three directions at all speeds. Under the same conditions, grinding force F_x decreased by 81.9%, grinding force F_y decreased by 74.0%, and grinding force F_z decreased by 77.2%.

Figure 6d–i shows the original signal curves (0.04 s in length) of two grinding methods at a speed of 7.85 m/s. The time for the abrasive particles to rotate half a circle is 0.004 s. The difference in the magnitude of the grinding force peaks was large, and the peak interval time was also different. It can be inferred that the peak force was the result of the interaction between the abrasive particles and SiC hard particles. Comparing Fig. 6d and i, it can be seen that, in the same time period, there were only 7 peaks in the grinding force signal for CG, and the maximum peak exceeded 20 N; while the number of peaks in the grinding force signal for UVAG exceeded 12, and the maximum peak grinding force did not exceed 5 N. Figure 6e and h, as well as Fig. 6f and i, also exhibited similar phenomena. That is to say, within the same grinding time (the same tangential length), the UVAG process results in a grinding force signal curve characterized by "high frequency and low value ", which may be related to the interaction between the abrasive particles and SiC hard particles.

In the simulation process of removing workpiece material with diamond abrasive particles, a single grinding force was formed due to the cutting and friction effects of the abrasive particles and the workpiece. The variation curve of the single grinding force (in the direction of the cutting path) is shown in Fig. 7a and b. It can be clearly seen that the single grinding force signal curve obtained from the simulation can be divided into two typical stages, namely, the removal stage of the matrix material and the removal stage of the

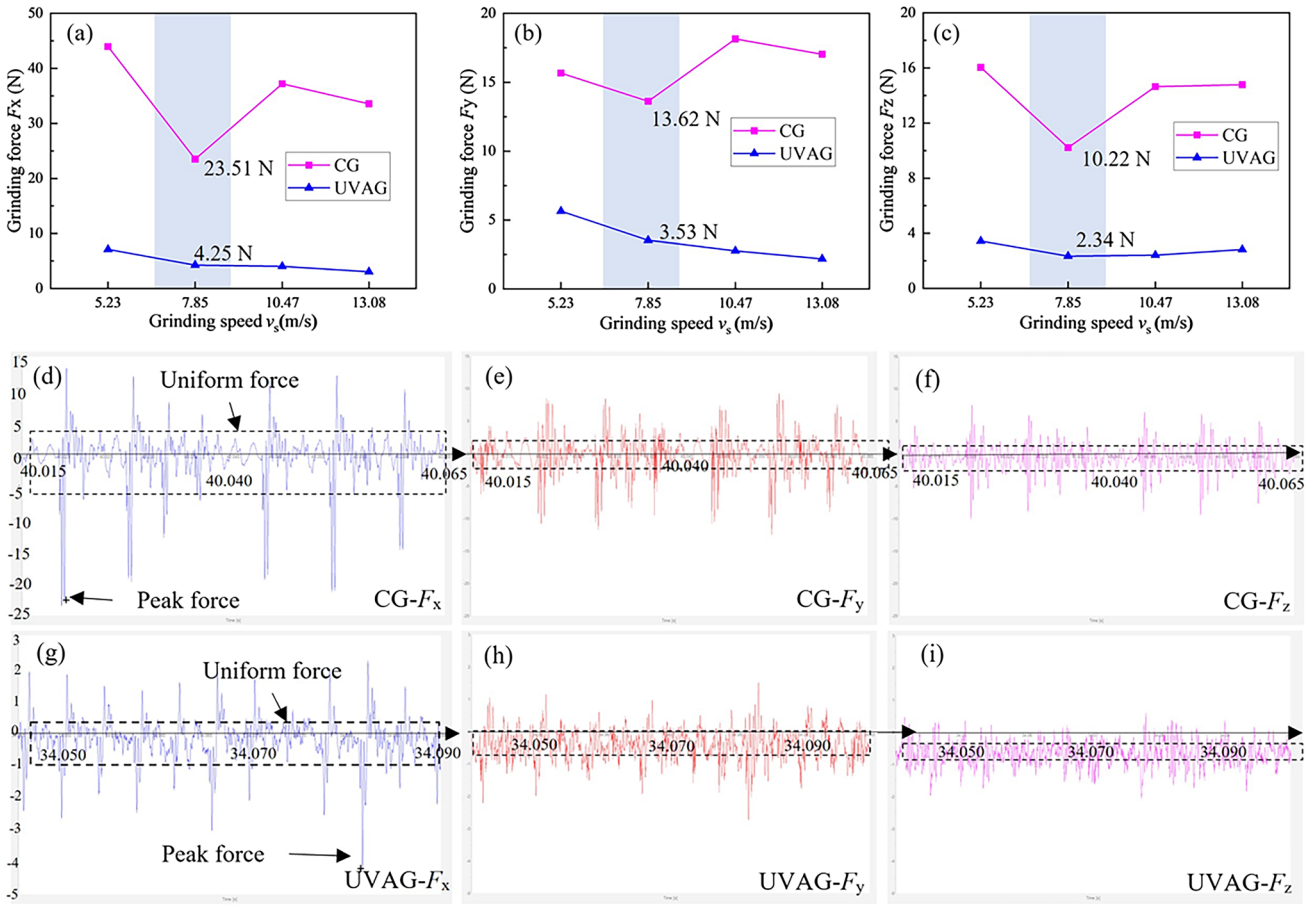

Fig. 6 Grinding forces of UVAG and CG under different grinding speeds **a** F_x, **b** F_y, and **c** F_z; **d–f** the intercepted CG force signal and **g–i** the intercepted UVAG force signal

reinforcement particles. The yellow rectangular box area in Fig. 7 is the removal stage of the reinforcement particles (particles 1 to 4), while the rest is the removal stage of the matrix material, during which the force signal remains basically stable. A cross-section is made within the XY plane, and this cross-section coincides with the central positions of the four SiC particles (Fig. 7c and d).

The red curve in Fig. 7a is the CG simulation force curve. During the removal of the base material, due to the continuous chip formation during the plastic removal process of the Al alloy, the variation amplitude of the single grinding force is relatively small, fluctuating around 2 N. However, during the removal of the reinforcement particles, the variation amplitude of the single grinding force significantly increased. When the abrasive particles were about to contact the reinforcement particles (point P1, Fig. 7c (P1)), the grinding force suddenly increased from 8.2 to 10.8 N. This is due to the high hardness of the reinforcement particles, and the shear slip of the chips is hindered by the SiC particles in the cutting path, resulting in an increase in grinding force and a peak value when the tool directly cuts the hard particles. At this time, micro-cracks are generated in the hard particles under the action of diamond abrasive particles. When the stress level of the material under high-speed extrusion reached the yield limit of the material, SiC particles began to fail brittly (point P2, Fig. 7c (P2)), and the grinding force suddenly dropped from 10.8 to 7.8 N. The reinforcement particles underwent brittle fracture, with significant crack propagation, and significant gaps appeared between the abrasive particles and reinforcement particles, causing a sudden drop in deformation resistance of the workpiece. As material removal progressed, when the abrasive particles again contacted the reinforcement particles (point P3, Fig. 7c (P3)), the grinding force rose again. When the reinforcement particles failed again (point P4), a brittle fracture occurred, and the grinding force dropped sharply again. Similar changes also occurred at positions P5 and P6 of particle 3 (Fig. 7c (P5 and P6)) and positions P7 and P8 of particle 4 (Fig. 7c (P7 and P8)). In addition, as the area of action between abrasive particles and particles increased, the holding ability of the Al matrix decreased, resulting in particle debonding and interfacial failure (Fig. 7c (P7 and P8)). It

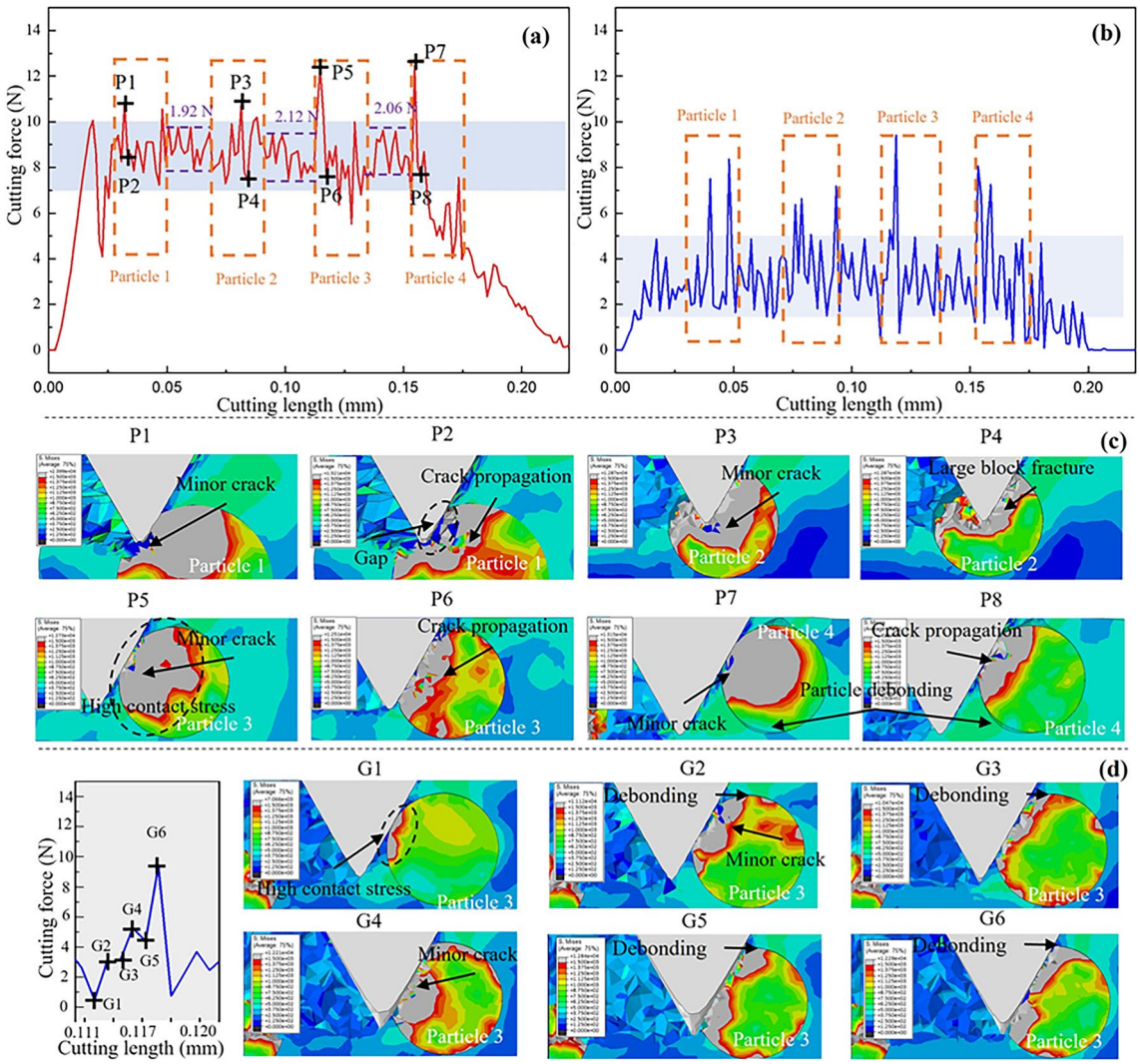

Fig. 7 Simulation grinding force curve and Mises stress distribution. **a** The variation curve of grinding force with cutting length under CG condition, **b** the variation curve of grinding force with cutting length under UVAG condition, **c** stress nephogram of marked points p1–p8 in (**a**), and **d** curve of the cutting force variation and the stress nephogram of marked points G1–G6 in (**b**)

can be seen that the distribution of SiC particles significantly impacts the instantaneous cutting force, exhibiting a distinct trend: an increase in the contact area between abrasive particles and reinforcement particles correlates directly with a higher peak grinding force.

Figure 7b depicts the force signal curve for UVAG, which reveals that during the metal matrix removal phase, the grinding force of UVAG is notably lower. Specifically, the primary grinding force values range from 1.5 to 5 N, significantly lower than the range of 7–10 N observed in CG (Fig. 7a). The reason is that ultrasonic vibration modified the initial continuous metal extrusion deformation cutting process during the matrix material removal process. This resulted in an intermittent, high-frequency extrusion deformation cutting process that allowed for the efficient separation of workpieces and abrasive particles, the timely cutting and discharging of plastic Al metal debris, the reduction of the cutting load, and the achievement of a decrease in grinding force. There was a noticeably larger change in the force of a single abrasive particle during the particle removal stage than during the matrix removal stage because of the high contact stress created by the high hardness of the reinforced particles between the diamond abrasive particle and the SiC-reinforced particles. Compared with stress cloud maps, when diamond abrasive particles came into contact with SiC particles, the high-stress area caused by UVAG was significantly smaller than that of CG (Fig. 7d (G1) compared to Fig. 7c (P5)), and the maximum stress also decreased significantly (G1 was 7.066×10^3 MPa, P5 was 1.273×10^4 MPa), avoiding large brittle fracture of particles under high contact stress. Therefore, thanks to high-frequency vibration perpendicular to the feed direction, the

removal volume of abrasive particles per cutting stroke was significantly reduced, enabling SiC particles to achieve high-frequency single micro-crushing (Fig. 7d (G1–G6)), while avoiding large-scale crack propagation and large-scale brittle fracture. At the same time, the debonding phenomenon on the bottom surface of SiC particles almost disappeared, with only slight debonding found on the top of particles directly in contact with abrasive particles (Fig. 7d (G2), (G3), (G5), and (G6)). This shows the "plastic-like removal" behavior of hard particles, which reduces the removal volume of SiC particles per vibration stroke, avoiding large-scale brittle fracture of traditional brittle particles, achieving a significant reduction in peak grinding force relative to that of CG, while also exhibiting a higher frequency of peak grinding force occurrence. This is similar to the "high-frequency and low-value" characteristic of the original grinding force acquisition signal shown in Fig. 6d–f.

3.1.2 Scratch morphologies

Figure 8 shows the 3D contour morphology of the surface at the initial stage of grinding. There were different degrees of particle bulges on the scratch bottom surface at different grinding speeds, which indicated that the hard SiC particles in the scratch track could not be completely removed under CG conditions. And relatively, at 7.85 m/s (Fig. 8b), the number of bulges was less and the height of bulges was lower, followed by 5.23 m/s (Fig. 8a), 13.08 m/s (Fig. 8d), and finally 10.47 m/s (Fig. 8c), which showed a positive relationship with the tangential grinding force F_y, proving that the larger the grinding force F_y, the greater the resistance encountered in the process of abrasive cutting movement, and the more difficult it was to effectively remove hard particles. The surface roughness at the bottom of the scratch also proved this point.

Figure 9 shows the trend of surface roughness of UVAG and CG under different grinding speeds. The length and width of 800 μm × 100 μm were intercepted from the bottom of the scratch in Fig. 8a–h. The surface roughnesses S_a were measured by Sansofar 3D profilometer. For CG, the surface roughness S_a exhibited a trend that was first declining and then increasing, and the minimum value was 1.45 μm at 7.85 m/s, reaching a minimum value of 1.45 μm at 7500 r/min and a maximum value of 3.67 μm at 10,000 r/min, which was consistent with the trend of the tangential cutting force F_y. From Fig. 8e–h, the bottoms of UVAG were smooth, the hard particles in the cutting path were completely removed, and there were no protruding particles in the path. The impact of grinding speed on the UVAG morphology was negligible, the change of surface roughness S_a

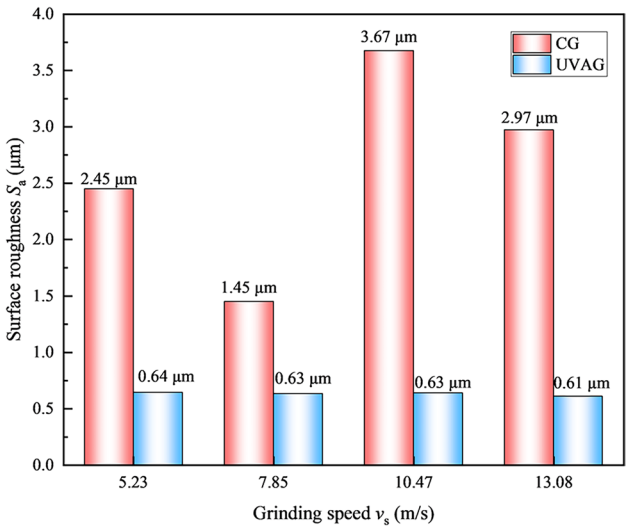

Fig. 9 Variation of surface roughness at the bottom of the scratch with grinding speed (red for CG; blue for UVAG)

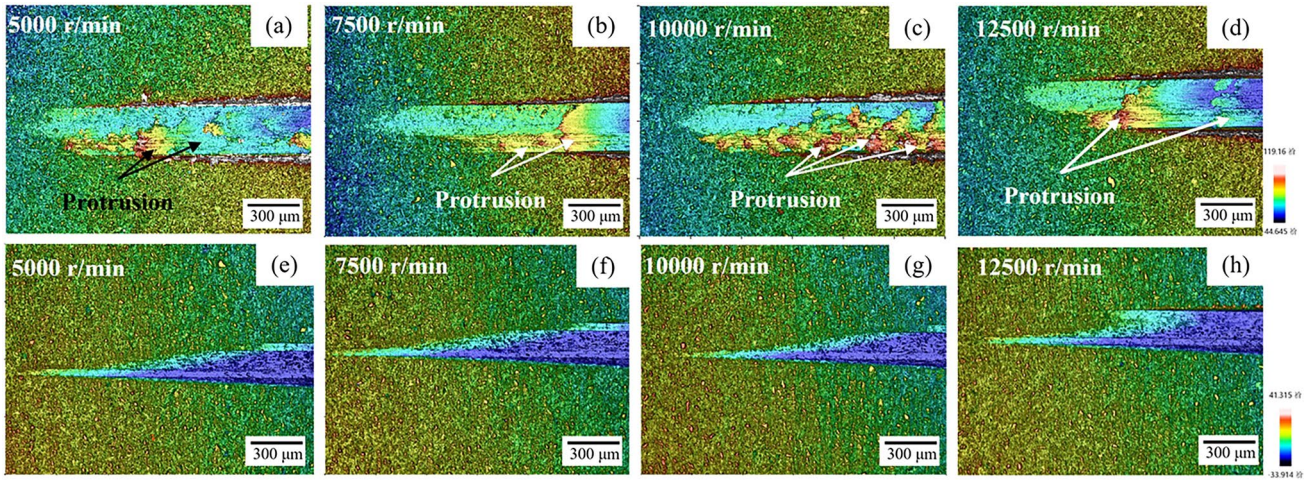

Fig. 8 Surface morphologies at the initial stage of grinding: CG (**a**–**d**) and UVAG (**e**–**h**)

was also small, and the trend was similar to that of tangential force F_y.

The morphology of the middle section of the scratch (Fig. 10) represents the main morphology after processing. Figure 10a shows the SEM morphology of CG, and the dark area on the bottom was the performance of the continuous "ironing" results of metal Al [31]. Under high-speed rotation, the particles were repeatedly extruded and rubbed in this area. Due to the plastic flow of the matrix material and the extrusion effect of the cutting edge, there was a coating phenomenon of the matrix material on the machined surface, which led to the smooth bottom surface, which masked the existence of some defects. However, this masking phenomenon did not appear continuously on the bottom surface. When the hard particles were crushed and removed by the tool, the ironing surface was torn and removed together. Figure 10b is the 3D morphology of Fig. 10a, in which the morphology of part of the scratch bottom surface, was put on Fig. 10c. It can be seen that there were a large number of irregular bulges on the bottom surface of CG morphology, which was considered to be the result of the adhesion and accumulation of the mixture (hard particles and metal binders) [32]. The primary reason behind this observation was the lack of timely chip discharge during the CG processing.

Figure 10d shows the SEM morphology of the scratch in the middle section of UVAG. The macro morphology of the scratch bottom surface was relatively smooth. From the micro perspective, it can be seen that there was particle shear and a large number of debris adhesions, and the plowing size and quantity were significantly reduced. This processing morphology was similar to the plastic removal morphology, but it was not the traditional plastic removal. Defects such as particle fracture and micro holes still affected the processing surface integrity of SiC_p/Al composites. Figure 10e is the 3D morphology of Fig. 10d, in which the morphology of part of the scratch bottom surface is put on Fig. 10f. It can be seen that the bottom surface of UVAG was smooth and almost free of bulges. Therefore, ultrasonic vibration significantly improved the removal ability of particle-reinforced composites, reduced the adhesion of Al matrix materials, and improved the machined surface quality.

Figure 11a shows the morphology of the bottom of CG, showing large particles adhering to the surface and plowing with large width and depth (width over 3 μm) This was the result of the secondary cutting of the material driven by abrasive particles after the SiC particles fell off or broke into large pieces. Irregular brittle fracture of SiC particles under stress resulted in crater morphology (Fig. 11b). When the interface stress exceeded the bonding strength of the interface phase, debonding and failure occurred at the interface (as depicted in Fig. 11c), ultimately leading to the complete detachment of SiC particles from the Al matrix and the

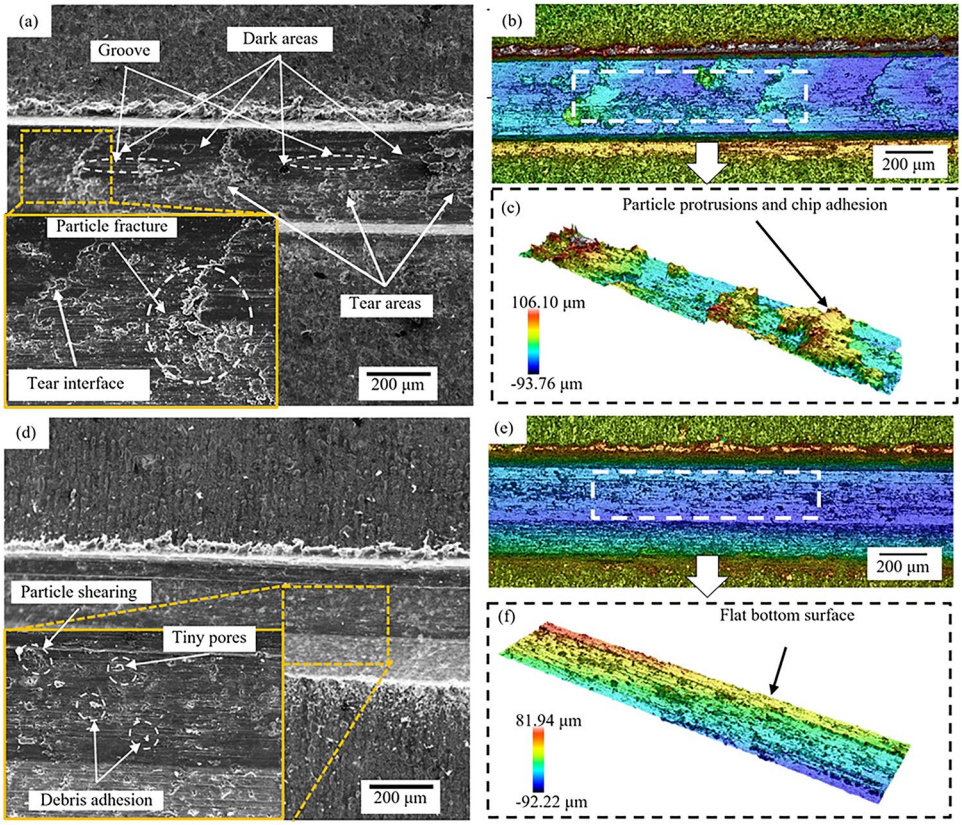

Fig. 10 Morphology of the scratch middle section. **a** SEM image of the scratch bottom surface of CG, **b** 3D contour of the scratch bottom of CG, **c** 3D morphology of the dotted selection of (**b**), **d** SEM image of the scratch bottom surface of UVAG, **e** 3D contour of the scratch bottom of UVAG, and **f** 3D morphology of the dotted selection of (**e**)

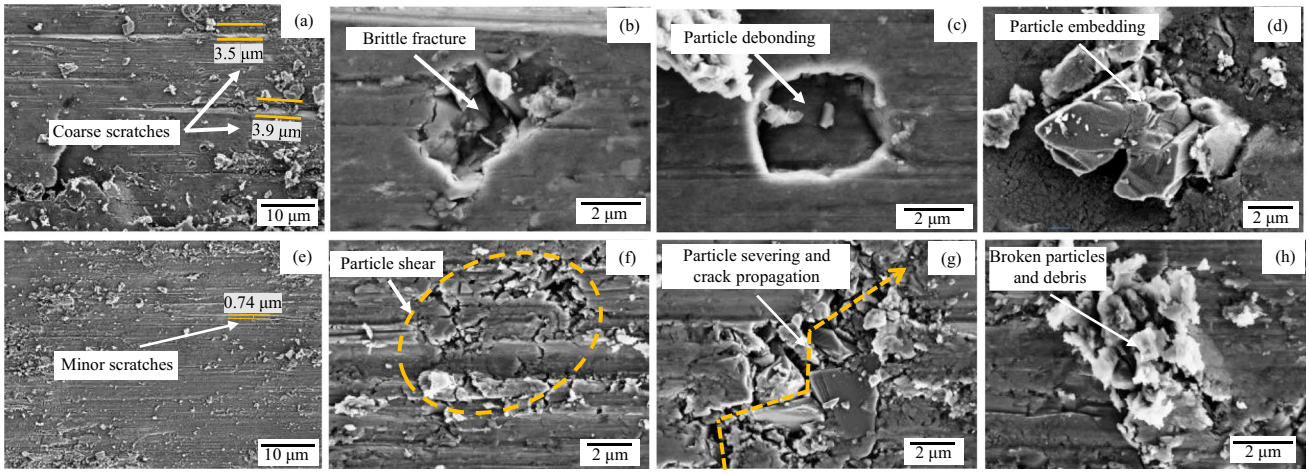

Fig. 11 Main machining defects of two grinding processes (**a**–**d** for CG and **e**–**h** for UVAG)

formation of pits on the machined surface. Figure 11d shows the broken bulk SiC particles separated from the machined surface and re-pressed into the matrix material under the action of tool extrusion. Since only a portion of the SiC chips were pressed into the matrix material, bulges were formed on the machined surface.

The UVAG bottom morphology (Fig. 11e) was greatly different from the CG grinding bottom morphology (Fig. 11a), mainly characterized by a large number of fine particles and fine scratches on the surface rather than coarse plowing. Figure 11f shows the morphology of particles cut off, showing a more complex cut surface phase than Fig. 11b, showing a multi-stage micro-fracture morphology. This was related to the reduction of single-pass cutting material volume by ultrasound-assisted machining [33] (single abrasive grain cutting thickness). Small cutting thickness can promote the transition of material removal from brittleness to plasticity [16, 34]. When SiC particles were gathered together, one particle was cut off, the strength of the surrounding metal matrix was reduced [25], and the resulting microcracks expanded to other particles under stress (Fig. 11g). Figure 11h shows the morphology of micro SiC fragments (different from the large-area fractured SiC in Fig. 11d) adhering to the machined surface with a metal chip mixture. Due to the friction and extrusion caused by the tool, the mixture ultimately adhered firmly to the machined surface.

Figure 12 is a cross-sectional view of FEM scribed morphology. Due to the existence of reinforcing particles, unique machined morphologies were obtained. For CG (Fig. 12a), the distribution of SiC particles had an important influence on the morphology formed after processing. When the cutting path passed through the upper part of the particle (particles 1 and 2), since the metal matrix still had sufficient holding force on the SiC particle after cutting, the force acting on the SiC particle exceeded the fracture criterion, the particle fracture morphology was formed, similar to Fig. 11b. When the cutting

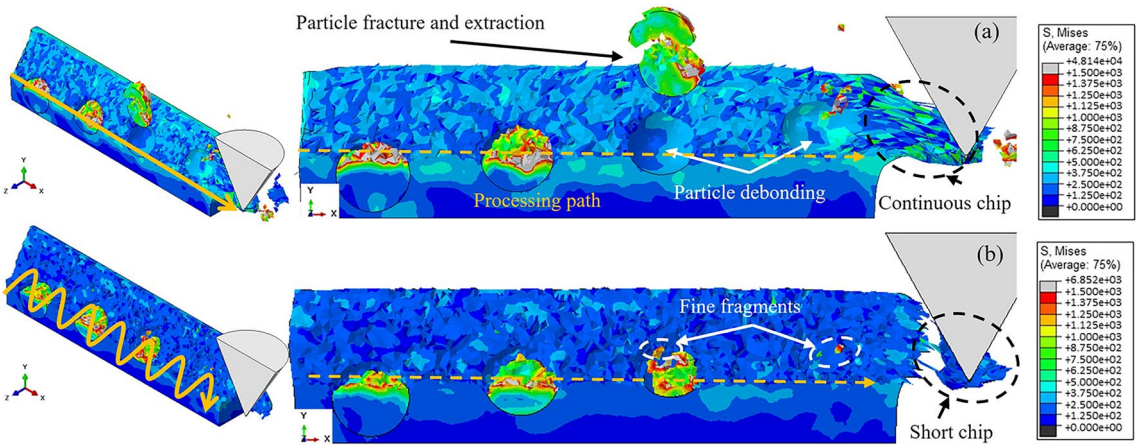

Fig. 12 Section of FEM grinding morphology: **a** CG and **b** UVAG

path passed through the lower part of the particle, the interface failure occurred at particles 3 and 4, the interface stresses were greater than the binding force of the interface phase, and the particle and the matrix were deboned to form holes, forming holes (similar to Fig. 11c). The subsequent shedding particle 3 may be discharged to form chips or may be pressed into the matrix surface by the continuous extrusion and friction of abrasive particles to form the morphology of Fig. 11d.

Figure 12b shows the section of UVAG simulation morphology. The residual stress of the workpiece after being scribed was smaller than that of CG. Particles 3 and 4 were machined to form a large number of tiny fragments rather than large particles in the cutting area, which was consistent with the morphological characteristics in Fig. 11e. This was because the ultrasonic processing of small single abrasive particle cutting thickness and instantaneous local impact effect [35, 36], which intensified the fracture and crushing of particles. Meanwhile, when abrasive particles acted on particle 3, the grinding force feature of "high frequency and low value" of ultrasonic-assisted machining effectively delayed the failure of the viscous interface and improved the machining surface integrity. In addition, from the shape of chips, ultrasonic machining can realize fast chip breaking of ductile metal when acting on Al base materials, and reduce the machining load.

The experiment and simulation results were summarized, and the material removal mechanisms under different abrasive particle movement modes can be obtained. The different classifications can be made according to the relative positions of abrasive particle and SiC particle contact, as shown in Fig. 13. For CG, when abrasive particles directly acted on SiC particles at a fast speed, as a brittle material under high contact stress, SiC particles will have a large area of brittle cracks, and then particle fracture will occur to form large pieces of SiC particles. When abrasive particles acted on the upper part of SiC, the Al matrix still had a strong holding force on SiC particles due to the large contact interface area of SiC-Al, so SiC particles were retained in the workpiece in the form of massive fracture (Fig. 13b). When abrasive particles acted below SiC, the SiC-Al contact interface area was greatly reduced, and the Al matrix had limited holding force on SiC particles, leading to large fracture of SiC particles, and SiC-Al contact interface began to fail, and SiC particles were pulled out and formed pits (Fig. 13b). Under the continuous extrusion friction of the subsequent abrasive particles, SiC particles were pressed into matrix combined with the softened Al, gradually accumulated, and formed bulge (Fig. 13c).

For UVAG, different from CG mode, abrasive grain received high-frequency vibration perpendicular to the feeding direction and acted on SiC particles in the inclined direction, reducing the action area of stress on SiC particles under single action, forming microcracks, completing the removal of SiC materials by multiple actions and forming

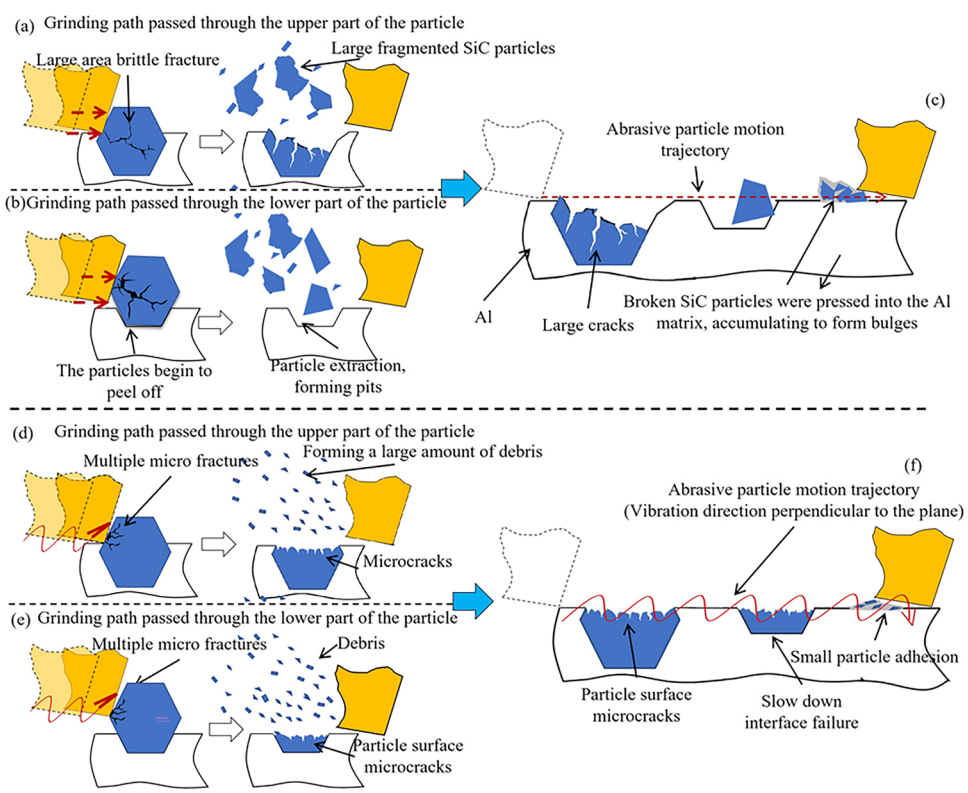

Fig. 13 Schematic diagram of material removal mechanism under different abrasive grain movement modes (**a**–**c** for CG and **d**–**f** for UVAG)

large amounts of tiny fragments. Therefore, the sections of SiC particles were relatively complete, showing the characteristics of plastic removal (Fig. 13d and e). The main features of UVAG were the reduction of the single contact area and the significant reduction of the contact stress, which reduced the impact on the SiC-Al contact interface and avoided the rapid interface failure (Fig. 13e). A small amount of small SiC fragments were combined with softened Al under the continuous extrusion friction effect of subsequent abrasive particles and adhered to the machined surface (Fig. 13f), avoiding excessive negative impact on the machining quality.

4 Conclusion

In this paper, the ultrasonic vibration-assisted machining and removal mechanism of SiC_p/Al composite was studied by carrying out grinding experiments and establishing FEM models. The material removal process and the contact state of abrasive particles with Al matrix and SiC-reinforced particles were analyzed systematically. This study provides a theoretical basis for the high-quality and efficient removal of Al matrix composites and facilitates their wider engineering applications. The main conclusions are as follows:

(1) Ultrasonic vibration significantly reduced the grinding force. As a kind of intermittent and high-frequency extrusion deformation cutting, the ultrasonic vibration can effectively separate the abrasive grain from the workpiece, timely cut off and discharge the plastic Al metal abrasive chips, and reduce the cutting load. On the other hand, UVAG enabled SiC particles to achieve high-frequency micro fragmentation, reducing the grinding force.

(2) The main factors affecting the surface quality of SiC_p/Al were the large-scale fragmentation and detachment of SiC particles, forming pits, and the adhesion and accumulation of the mixture of fragmented SiC particles and Al metal chips. UVAG promoted the "pseudoplastic" removal of SiC particles, and the processing had a smaller contact stress and action area, effectively reducing damage to the bonding interface.

(3) The SiC particles had a secondary cutting effect on the material in both processes. In CG, the broken large SiC particles push and cut the Al matrix, forming a small number of plows with large width and depth. For UVAG, the thickness of a small single abrasive grain made SiC particles form a large number of tiny fragments, and the machining surface was mainly characterized by fine scratches, which improved the integrity of the machining surface.

Author contribution Jianhao Peng: experimentation, data curation, and writing the original draft. Yu Yao: experimentation and methodology. Zhipeng Xu: resources. Xuebin Yao: experimentation and methodology. Biao Zhao: data collection and manuscript revision. Wenfeng Ding: supervision, conceptualization, and methodology.

Funding This work was financially supported by the National Natural Science Foundation of China (Nos. 92160301, 92060203, 52175415, and 52205475), the Science Center for Gas Turbine Project (No. P2023-B-IV-003–001), the Natural Science Foundation of Jiangsu Province (No. BK20210295), the Huaqiao University Engineering Research Center of Brittle Materials Machining (No. 2023IME-001), the Fundamental Research Funds for the Central Universities (No. NS2023028), and the Postgraduate Research and Practice Innovation Program of Jiangsu Province (No. KYCX24_0549).

Data availability All data generated or analyzed during this study are included in the present article.

Declarations

Ethics approval and consent to participate The article follows the guidelines of the Committee on Publication Ethics (COPE) and involves no studies on human or animal subjects.

Consent to participate Not applicable.

Consent for publication Not applicable.

Competing interests The authors declare no competing interests.

References

1. Lu SX, Gao H, Bao YG, Xu QH (2019) A model for force prediction in grinding holes of SiC_p/Al composites. Int J Mech Sci 160:1–14. https://doi.org/10.1016/j.ijmecsci.2019.06.025
2. Zhao B, Peng JH, Ding WF (2023) Machined surface formation and integrity control technology of SiC_p/Al composites: a review. Surf Sci Technol 1:10. https://doi.org/10.1007/s44251-023-00011-8
3. Laghari RA, Jamil M, Laghari AA, Khan AM, Akhtar SS, Mekid S (2023) A critical review on tool wear mechanism and surface integrity aspects of SiC_p/Al MMCs during turning: prospects and challenges. Int J Adv Manuf Technol 126:2825–2862. https://doi.org/10.1007/s00170-023-11178-7
4. Zhang L, Xu HQ, Wang Z, Li QG, Wu JY (2016) Mechanical properties and corrosion behavior of Al/SiC composites. J Alloy Compd 678:23–30. https://doi.org/10.1016/j.jallcom.2016.03.180
5. Zhou M, Wang M, Dong GJ (2016) Experimental investigation on rotary ultrasonic face grinding of SiC_p/Al composites. Mater Manuf Processes 31:673–678. https://doi.org/10.1080/10426914.2015.1025962
6. Wang ZY, He YJ, Yu TB (2022) Surface quality and milling force of SiC_p/Al ceramic for ultrasonic vibration-assisted milling. Ceram Int 48:33819–33834. https://doi.org/10.1016/j.ceramint.2022.07.331
7. Gao L, Liu C, Liu J, Yang T (2023) Effect of subsurface damage on tensile behavior and fracture mechanism of SiC_p/Al composites: experimental analysis and RVE modeling. Eng Fail Anal 147:107162. https://doi.org/10.1016/j.engfailanal.2023.107162
8. Xiang DH, Li B, Peng PC, Shi ZL, Li YQ, Gao GF, Zhao B (2021) Study on formation mechanism of edge defects of high-volume fraction SiC_p/Al composites by longitudinal-torsional ultrasonic

vibration-assisted milling. Proc Inst Mech Eng C J Mech Eng Sci 236:6219–6231. https://doi.org/10.1177/09544062211065634
9. Zhou JK, Lu MM, Lin JQ, Zhou XQ, Guo MQ, Du YS (2022) Investigation of surface integrity transition of SiC_p/Al composites based on specific cutting energy during ultrasonic elliptical vibration assisted cutting. J Manuf Process 79:654–665. https://doi.org/10.1016/j.jmapro.2022.04.067
10. Lu SJ, Zhang JJ, Li ZQ, Zhang JG, Wang XH, Hartmaier A, Xu JF, Yan YD, Sun T (2021) Cutting path-dependent machinability of SiC_p/Al composite under multi-step ultra-precision diamond cutting. Chin J Aeronaut 34:241–252. https://doi.org/10.1016/j.cja.2020.07.039
11. Zhao B, Ding WF, Shan ZD, Wang J, Yao CF, Zhao ZC, Liu J, Xiao SH, Ding Y, Tang XW, Wang XC, Wang YF, Wang X (2023) Collaborative manufacturing technologies of structure shape and surface integrity for complex thin-walled components: status, challenge and tendency. Chin J Aeronaut 36(7):1–24. https://doi.org/10.1016/j.cja.2023.02.008
12. Zhao B, Wu BF, Yue YS, Ding WF, Xu JH, Guo GQ (2023) Developing a novel radial ultrasonic vibration-assisted grinding device and evaluating its performance in machining PTMCs. Chin J Aeronaut 36(7):244–256. https://doi.org/10.1016/j.cja.2023.01.008
13. Ying J, Yin Z, Zhang P, Zhou PX, Zhang K, Liu ZH (2022) An experimental study of the surface roughness of SiC_p/Al with ultrasonic vibration-assisted grinding. Metals 12:1730
14. Wang YF, Liao WH, Yang K, Chen WQ, Liu TT (2019) Investigation on cutting mechanism of SiC_p/Al composites in precision turning. Int J Adv Manuf Technol 100:963–972. https://doi.org/10.1007/s00170-018-2650-1
15. Du JG, Ming WY, Cao Y, Ma J, He WB, Li XK (2019) Particle removal mechanism of high volume fraction SiC_p/Al composites by single diamond grit tool. J Wuhan Univ Technol Mater Sci Ed 34:324–331. https://doi.org/10.1007/s11595-019-2055-5
16. Feng PF, Liang GQ, Zhang JF (2014) Ultrasonic vibration-assisted scratch characteristics of silicon carbide-reinforced aluminum matrix composites. Ceram Int 40(7):10817–10823. https://doi.org/10.1016/j.ceramint.2014.03.073
17. Zhang YZ, Fang CF, Huang GQ, Xu XP (2018) Modeling and simulation of the distribution of undeformed chip thicknesses in surface grinding. Int J Mach Tools Manuf 127:14–27. https://doi.org/10.1016/j.ijmachtools.2018.01.002
18. Lu SJ, Li ZQ, Zhang JJ, Sun T (2023) Revealing cutting mode transition in diamond cutting of SiC_p/Al based on specific cutting energy model. Int J Adv Manuf Technol 129:909–922. https://doi.org/10.1007/s00170-023-12318-9
19. Zheng W, Wang YJ, Zhou M, Wang Q, Ling L (2018) Material deformation and removal mechanism of SiC_p/Al composites in ultrasonic vibration assisted scratch test. Ceram Int 44(13):15133–15144. https://doi.org/10.1016/j.ceramint.2018.05.150
20. Gu P, Zhu CM, Sun YC, Wang Z, Tao Z, Shi ZQ (2023) Surface roughness prediction of SiC_p/Al composites in ultrasonic vibration-assisted grinding. J Manuf Process 101:687–700. https://doi.org/10.1016/j.jmapro.2023.05.093
21. Yuan ZJ, Xiang DH, Peng PC, Zhang ZQ, Li BH, Ma MY, Zhang ZZ, Li BH, Ma MY, Zhang ZP, Gao GF, Zhao B (2023) A comprehensive review of advances in ultrasonic vibration machining on SiC_p/Al composites. J Market Res 24:6665–6698. https://doi.org/10.1016/j.jmrt.2023.04.245
22. Zhao GL, Zhao B, Ding WF, Xin LJ, Nian ZW, Peng JH, He N, Xu JH (2024) Nontraditional energy-assisted mechanical machining of difficult-to-cut materials and components in aerospace community: a comparative analysis. Int J Extreme Manuf 6:022007
23. Zha HT, Feng PF, Zhang JF, Yu DW, Wu ZJ (2018) Material removal mechanism in rotary ultrasonic machining of high-volume fraction SiC_p/Al composites. In J Adv Manuf Technol 97(5–8):2099–2109. https://doi.org/10.1007/s00170-018-2075-x
24. Li B, Xiang DH, Peng PC, Li YQ, Liu GF, Gao GF, Zhao B (2023) Experimental and FEM study of surface formation and deformation mechanism of SiC_p/Al composites in laser-ultrasonic vibration assisted turning. Ceram Int 49(9):13510–13519. https://doi.org/10.1016/j.ceramint.2022.12.226
25. Yu WW, Chen J, Ming WW, An QL, Chen M (2021) Experimental and FEM study of cutting mechanism and damage behavior of ceramic particles in orthogonal cutting SiC_p/Al composites. Ceram Int 47(5):7183–7194. https://doi.org/10.1016/j.ceramint.2020.11.072
26. Chen Y, Gao Q, Wang QZ, Yin XY (2023) Simulation and experimental study on milling mechanism and tool wear of low volume SiC_p/Al composites. Proc Inst Mech Eng C J Mech Eng Sci 237:4271–4283. https://doi.org/10.1177/09544062221148422
27. Anderson D, Warkentin A, Bauer R (2011) Experimental and numerical investigations of single abrasive-grain cutting. Int J Mach Tools Manuf 51:898–910. https://doi.org/10.1016/j.ijmachtools.2011.08.006
28. Jiang XD, Xiao DH, Teng XY (2022) Influence of vibration parameters on ultrasonic vibration cutting micro-particles reinforced SiC/Al metal matrix composites. Int J Adv Manuf Technol 119:6057–6071
29. Zhang ZW, Men XH, Pan YZ, Wang ZD, Shi QH, Fu XL (2022) Research on simulation of SiC_p/Al finite element cutting based on cohesive model. Mater Today Commun 32:103848. https://doi.org/10.1016/j.mtcomm.2022.103848
30. Zhou YG, Liu J, Wang SH, Chen H, Li DZ, Ma LJ, Li M (2024) Study on the removal mechanism and milling quality of helical milling hole of SiC_p/Al composites. J Manuf Process 109:379–393. https://doi.org/10.1016/j.jmapro.2023.12.04
31. Dong ZG, Zheng FF, Zhu XL, Kang RK, Zhang B, Liu ZQ (2017) Characterization of material removal in ultrasonically assisted grinding of SiC_p/Al with high volume fraction. Int J Adv Manuf Technol 93:2827–2839. https://doi.org/10.1007/s00170-017-0676-4
32. Yin GQ, Wang D, Cheng J (2019) Experimental investigation on micro-grinding of SiC_p/Al metal matrix composites. Int J Adv Manuf Technol 102:3503–3517. https://doi.org/10.1007/s00170-019-03375-0
33. Zhang K, Yin Z, Dai CW, Miao Q, Cheng QH (2022) Undeformed chip thickness characteristics in grain-workpiece contact zone in ultrasonic vibration assisted grinding. Diamond Abrasives Eng 42(1):88–96. https://doi.org/10.13394/j.cnki.jgszz.2021.0109
34. Gao XX, Yuan SM, Li Q, Chen BC, An WZ, Wang LY (2024) Ductile-brittle transition mechanism of SiC particle-reinforced Al-MMCs under ultrasonic assisted grinding with single grain. J Market Res 28:3655–3669. https://doi.org/10.1016/j.jmrt.2023.12.252
35. Miao Q, Ding WF, Chen T, Zhao B, Qian N, Dai CW, Yin Z (2024) Surface gradient structures in single-crystal nickel alloy induced by ultrasonic-assisted high-speed grinding. Mater Today Commun 38:107930. https://doi.org/10.1016/j.mtcomm.2023.107930
36. Cao Y, Ding WF, Zhao B, Wen XB, Li SP, Wang JZ (2022) Effect of intermittent cutting behavior on the ultrasonic vibration-assisted grinding performance of Inconel718 nickel-based superalloy. Precis Eng J Int Soc Precis Eng Nanotechnol 75:248–260. https://doi.org/10.1016/j.precisioneng.2022.08.006

Publisher's Note Springer Nature remains neutral with regard to jurisdictional claims in published maps and institutional affiliations.

Springer Nature or its licensor (e.g. a society or other partner) holds exclusive rights to this article under a publishing agreement with the author(s) or other rightsholder(s); author self-archiving of the accepted manuscript version of this article is solely governed by the terms of such publishing agreement and applicable law.